Front. Struct. Civ. Eng. 2021, 15(1): 147–166
https://doi.org/10.1007/s11709-020-0704-6

RESEARCH ARTICLE

# Model test and discrete element method simulation of shield tunneling face stability in transparent clay

**Huayang LEI[a,b,c], Yajie ZHANG[a], Yao HU[a*], Yingnan LIU[a]**

[a] *School of Civil Engineering, Tianjin University, Tianjin 300350, China*

[b] *Key Laboratory of Coast Civil Structure Safety (Tianjin University), Ministry of Education, Tianjin 300350, China*

[c] *Key Laboratory of Earthquake Engineering Simulation and Seismic Resilience of China Earthquake Administration (Tianjin University), Tianjin 300350, China*

[*] *Corresponding author. E-mail: huyao@tju.edu.cn*



**ABSTRACT** The stability of the shield tunneling face is an extremely important factor affecting the safety of tunnel construction. In this study, a transparent clay with properties similar to those of Tianjin clay is prepared and a new transparent clay model test apparatus is developed to overcome the "black box" problem in the traditional model test. The stability of the shield tunneling face (failure mode, influence range, support force, and surface settlement) is investigated in transparent clay under active failure. A series of transparent clay model tests is performed to investigate the active failure mode, influence range, and support force of the shield tunneling face under different burial depth conditions, whereas particle flow code three-dimensional numerical simulations are conducted to verify the failure mode of the shield tunneling face and surface settlement along the transverse section under different burial depth conditions. The results show that the engineering characteristics of transparent clay are similar to those of soft clay in Binhai, Tianjin and satisfy visibility requirements. Two types of failure modes are obtained: the overall failure mode (cover/diameter: $C/D \leqslant 1.0$) and local failure mode ($C/D \geqslant 2.0$). The influence range of the transverse section is wider than that of the longitudinal section when $C/D \geqslant 2.0$. Additionally, the normalized thresholds of the relative displacement and support force ratio are 3%–6% and 0.2–0.4, respectively. Owing to the cushioning effect of the clay layer, the surface settlement is significantly reduced as the tunnel burial depth increases.

**KEYWORDS** shield tunneling face, stability, transparent clay, model test, numerical simulation

## 1 Introduction

Owing to rapid economic development, many cities in China are planning to increase metro line construction. In the construction of urban subway tunnels, the most typical construction method is the shield tunneling method. As an important factor affecting the safety of shield tunneling construction, the stability of the shield tunneling face is extremely important to engineers and researchers. During the excavation of the shield, a slurry or earth pressure is used on the work face to support the surrounding soils. If the support parameters of the shield tunneling face are set improperly, the active or passive earth pressure will change, and in severe cases, instability and damage will occur, resulting in serious engineering accidents.

In the past decades, studies regarding modern shield tunneling construction have been conducted, providing a foundation for subsequent related studies. Currently, research methods to investigate the stability of shield tunneling face primarily include theoretical analysis, model testing, and numerical simulation. In terms of theoretical analysis, Horn [1] first proposed a three-dimensional failure model with a wedge shape and a rectangular parallelepiped based on the limit equilibrium method. Subsequently, some scholars improved the three-dimensional failure model and established limit equilibrium models for the stability analysis of shield tunneling face [2–6]. Furthermore, some scholars deduced the limit values of active and passive earth pressure using the limit analysis or limit equilibrium method during failure [7–10].

*Article history: Received Mar 13, 2020; Accepted Apr 19, 2020*

Using these methods, shield construction parameters can be determined.

The traditional model test offers distinct advantages and is widely used to investigate the stability of the shield tunneling face. The primary methods used in model tests are constant gravity model tests [11–13] and centrifuge tests [14,15]. However, the traditional model tests to investigate the stability of the shield tunneling face present two main disadvantages. First, the traditional model tests damage the original structure of the natural soil and affect the dynamic response of the soil and deformation field by inserting a sensor. Second, the traditional model test presents the "black box" problem. The natural soil used in the test is not visible; therefore, the internal deformation of the shield tunneling face cannot be directly observed.

Hence, some scholars use numerical calculation software to perform further investigations. Typically used numerical simulations can be classified into two categories: the finite element method (FEM) and the discrete element method (DEM). Many experts have obtained cutting-edge research results using the FEM in geotechnical engineering [16–18]. Considering the movement law of soil particles during the failure process, many scholars have used the DEM for numerical simulation [19–23]. Recently, a new high efficiency and robustness method termed "discontinuity layout optimization" has been successfully applied for analyzing the stability of shield tunneling construction [24–26], and a new approach for modeling discrete cracks in mesh-free methods has been proposed to solve discontinuities and fractures [27,28]. Numerical simulations have significantly promoted research development. However, because numerical simulations are not identical to the actual project, the real situation cannot be reflected accurately in the former.

With the advancement of materials science, a new research method for transparent soil has been applied. Some scholars used transparent silica to simulate natural sand and verified its feasibility. The production of transparent soil can be traced back to Mannheimer and Oswald [29]. Subsequently, some scholars confirmed that transparent silica can simulate sand [30–33]. Transparent soil has been used to simulate various underground engineering problems, including foundation drainage [34,35], shallow foundations [36,37], tunnel face stability [38], and ground movement induced by tunneling [39]. Previous studies [40–42] investigating the stability of the shield tunneling face is primarily based on transparent sand. Because transparent clay is difficult to prepare, research pertaining to it is scarce. Nevertheless, many construction projects are performed in clay foundations, and transparent clay must be produced to simulate natural clay.

This paper describes the stability (active failure mode, influence range, support force, and surface settlement) of the shield tunneling face under different burial depth conditions via transparent clay model tests and particle flow code three-dimensional ($PFC^{3D}$) numerical simulations. This study presents two unique aspects: first, combined with the engineering characteristics of Tianjin soft clay, a new transparent clay model test apparatus is developed to overcome the "black box" problem in traditional model tests and the internal displacement of the soil can be directly observed under an active failure; second, the active failure model of the shield tunneling face is revealed from the longitudinal and transverse sections, whereas the failure shape and influence range are analyzed using an accurate function. In addition, the $PFC^{3D}$ software is employed to simulate the internal movement of soil particles, and the surface settlement is analyzed comparatively for active failure.

The remainder of this paper is organized as follows. We used amorphous silicon powder, #15 white oil, and *n*-dodecane to prepare transparent clay, and its visibility and similarity with soft clay from Binhai in Tianjin was proven through a series of triaxial tests, as will be explained in Section 2. Subsequently, we introduce a self-developed transparent soil model test apparatus and a test scheme to study the active failure mode of shield tunneling face in Section 3. We performed transparent clay model tests to study the active failure mode, influence range, and threshold support force of the shield tunneling face along the longitudinal and transverse sections at different depths, as will be presented in Section 4. In Section 5, we present the $PFC^{3D}$ numerical simulation conducted to verify the failure mode and surface settlement of the shield tunneling face. Finally, we provide the conclusions regarding our study in Section 6.

## 2 Experimental materials and equipment

### 2.1 Experimental materials

To observe the internal deformation of the soil, transparent clay was selected as the test material in this study. Transparent clay comprises three primary materials: amorphous silicon powder, #15 white oil, and *n*-dodecane. Amorphous silicon powder was used as the solid phase material, and #15 white oil and *n*-dodecane were used as the pore fluids. The physical parameters are listed in Table 1. In terms of solid particles, the particle size of the solid particles (amorphous silica powder) in transparent

**Table 1** Physical parameters of the material

| material | physical parameters |
|---|---|
| amorphous silicon powder | particle size: 4–10 μm; dry density: 0.056–0.230 g/cm$^3$ |
| #15 white oil | viscosity: 13.5–16.5 mm$^2$/s (20°); density: 0.848 g/cm$^3$ |
| *n*-dodecane ($C_{12}H_{26}$) | melting point: –9.6°C; boiling point: 215°C–217°C |

clay was between 4 and 10 μm, which is the particle size range of clay. Therefore, amorphous silicon powder is suitable for simulating actual clay particles. According to Lei et al. [43], the optimal ratios of transparent clay at laboratory temperature (20°C) is #15 white oil: *n*-dodecane = 10:3 (volume ratio) and pore fluid: amorphous silicon powder = 1.5:1 (mass ratio).

When preparing transparent clay, the small particle size of the amorphous silicon powder will result in a large number of bubbles, which are not easy to dissipate, thereby affecting the visibility of transparent clay and necessitating gentle stirring and vacuuming. In addition, temperature significantly affects the visibility of transparent clay [44]; therefore, the laboratory temperature must be maintained at approximately 20°C.

Transparent clay possesses extremely high visibility when the optimal ratio is used, and its physical and mechanical properties are similar to those of soft clay in Binhai, Tianjin. The visibility of the prepared transparent clay is shown in Fig. 1. Because of the different shooting positions (as shown in Figs. 1(a) and 1(c)), the "transparent soil" gray value was used in this study to determine the visibility. The range of gray value is generally from 0 to 255, where 0 and 225 represent pure black and pure white, respectively. The gray values in Figs. 1(a) and 1(c) are 65 and 103, respectively. Based on the gray value in Fig. 1(a), the gray value percentage in Fig. 1(c) is 72%. It can be concluded that the visibility depicted in Fig. 1(c) is approximately 70% that of Fig. 1(a), indicating compliance with testing requirements.

Through a series of tests, the physical and basic mechanical indicators of the transparent clay used in this study were obtained. In addition, other natural clay physical property indicators are summarized herein based on other relevant articles, as shown in Table 2. In terms of the density characteristics, the density of transparent clay is approximately 1.40 g/cm$^3$, which is 60%–70% that of natural clay. The values of cohesion ($c$) and friction angle ($\varphi$) of the transparent clay were consistent with those of silty clay in Binhai, Tianjin. The compression characteristics of the transparent clay and Tianjin silty clay were similar, and the basic physical properties were the same except for the density and water (oil) rate. The difference between the compression factor and compression modulus was within 10%. Hence, it was demonstrated that transparent clay is feasible for simulating natural clay.

To determine the material similarity of transparent clay and natural clay, consolidated undrained shear tests were designed for both clay materials, and the stress-strain curves were normalized, i.e., the data points on the curve were divided by the maximum value on the curve. The normalized stress-strain relationship curve is shown in Fig. 2. As shown in the figure, transparent clay is highly similar to natural clay. In summary, the transparent clay prepared in this study satisfied the conditions for simulating natural clay.

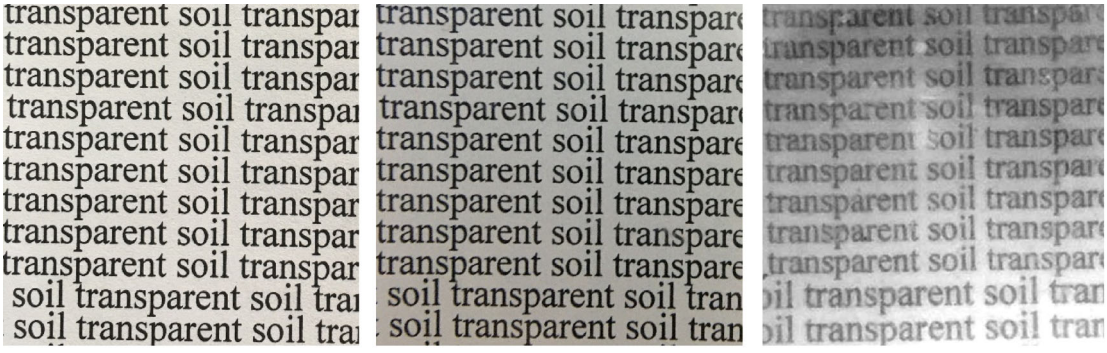


**Fig. 1** Comparison of visibility in different media: (a) air; (b) glass; (c) transparent clay.

**Table 2** Physical and basic mechanical property comparison [43]

| source of soil | transparent clay in this paper | silty clay in Binhai, Tianjin [45] | Ariake clay [46] | Kitakyushu clay [47] |
|---|---|---|---|---|
| density $\rho$ (g·cm$^{-3}$) | 1.4 | 1.757 | – | – |
| water (oil) rate $\omega$ (%) | 150 | 50.3 | 87.4 | 59.4 |
| initial porosity $e_0$ | 1.306 | 1.34 | 2.25 | 1.582 |
| compression factor $a_{1-2}$ (MPa$^{-1}$) | 0.868 | 0.81 | 3.8 | 1.6 |
| compression modulus $E_{s(0.1\text{-}0.2)}$ (MPa) | 2.543 | 2.81 | 0.855 | 1.614 |
| cohesion $c$ (kPa) | 11.7–22.62 | 17.6 | – | – |
| internal friction angle $\varphi$ | 14.19°–18.65° | 9.3° | – | – |

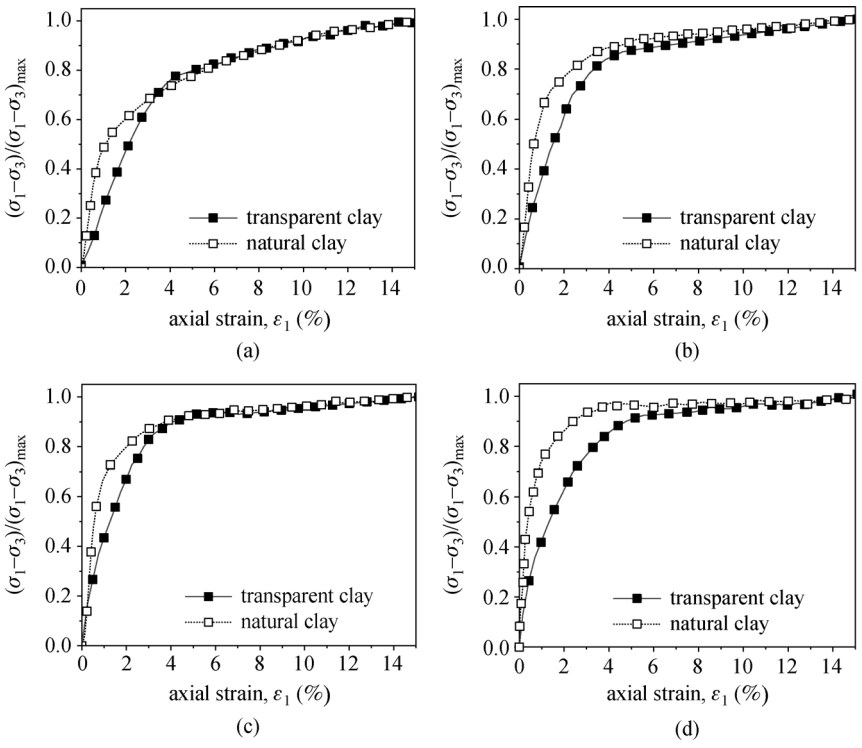


**Fig. 2** Normalized triaxial compression curves between transparent clay and natural clay: (a) 100 kPa confining pressure; (b) 200 kPa confining pressure; (c) 300 kPa confining pressure; (d) 400 kPa confining pressure.

## 2.2 Test apparatus of model test

Two methods of model testing can be used to investigate the stability of the shield tunneling face: the force method (changes in force cause changes in displacement) and displacement method (changes in displacement cause changes in force). Owing to the principle of the self-developed test apparatus (the support end moves backward to simulate the process of active failure) in this study, the displacement method was adopted, from which the threshold support force was obtained. The test method was based on Ahmed and Iskander [30], who were the first to propose the use of this method in a transparent sand experiment.

Figure 3(a) shows the test apparatuses used in this study; they primarily include the following five components:

1) model test box: model test chamber (25 cm × 25 cm × 40 cm); plexiglas base (length × width = 40 cm × 40 cm);

2) shield tunneling face moving apparatus: shield tunneling face moving apparatus ($\Phi$ = 5 cm); support force monitor;

3) optical test platform: sliding rail (length $l$ = 1.5 m); self-balancing optical platform (1.5 m × 2 m);

4) visual image acquisition system: laser (200 MW, 650 nm); industrial camera (resolution 4896 × 3264); laser bracket; camera stand;

5) particle image velocimetry (PIV) analysis software.

This set of test apparatuses enable large deformation and instability condition simulations of shield tunneling faces as well as realize the dynamic monitoring and analysis of the instability process of shield tunneling faces by combining laser section images and digital image analysis technology.

Figure 3(b) shows the shield tunneling face moving apparatus. A screw was used in the apparatus to connect the end face of the shield tunneling face and the flange of the sidewall of the model box. The spiral handle was arranged outside the flange, enabling the shield tunneling face to be retreated by rotating the handle. A pressure sensor was arranged at the end to monitor the change in the support force when the shield tunneling face exhibited instability (Fig. 3(c)).

The tracer particles used in the test were hollow glass microspheres manufactured by the 3M Company in the United States, and model iM16K with a particle size of 12–20 μm and a density of 0.6 g/cm$^3$ was used. The displacement field analysis software used in this study was PIV view2C (PIV view2C) developed by the German Aerospace Center. Figure 3(d) shows a schematic illustration of the PIV technique, which can be used to perform a displacement field analysis on the image of soil near the captured face of the shield. When investigating the failure mode of the transverse section, the laser light irradiated to the edge of the plexiglass tube will distort the captured image. Therefore, in this study, the laser was shifted 2 mm

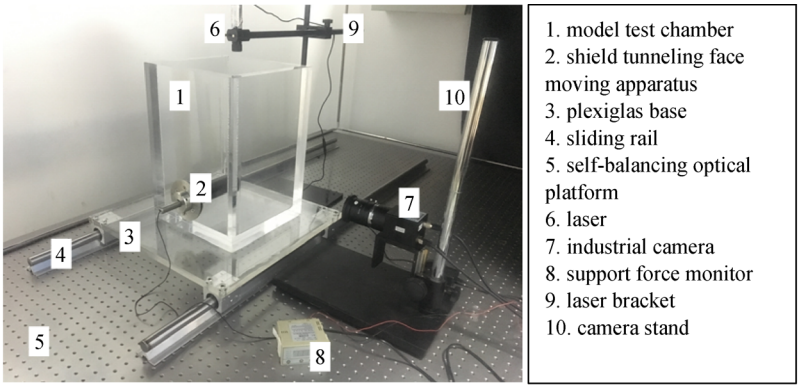


(a)

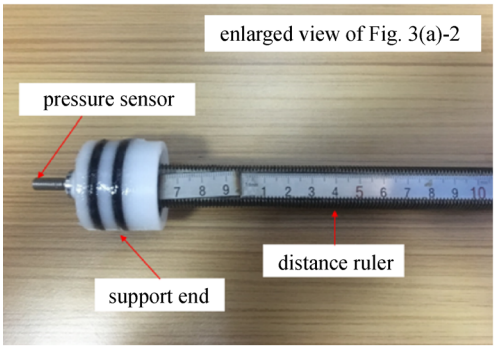


(b)


(c)

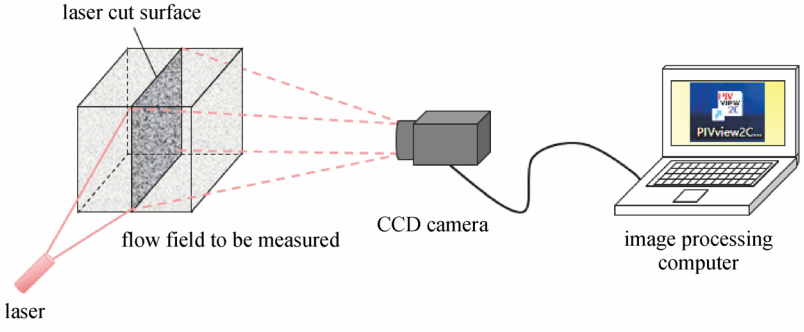


(d)

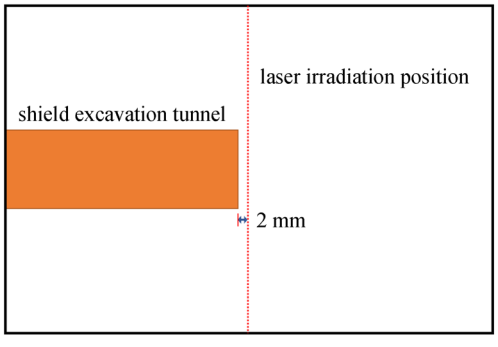


(e)

**Fig. 3** Test apparatus: (a) test schematic; (b) shield tunneling face moving apparatus; (c) support force monitor; (d) schematic diagram of the PIV system; (e) longitudinal section of model box.

directly in front of the shield tunneling face, as shown in Fig. 3(e). The laser-cut surface at this position is the transverse section.

## 3 Test scheme and procedure

### 3.1 Test scheme

The burial depth of the tunnel is an important factor affecting the stability of the shield tunneling face. The test was designed based on factors such as the tunnel depth ratio $C/D$ and the position of the monitoring section. The stability of the shield tunneling face under different burial depth conditions was analyzed. Additionally, corresponding numerical simulations were performed for each model test. The specific test scheme is shown in Table 3.

**Table 3** Scheme of the model test and numerical simulation

| test id | monitored section | cover/diameter ($C/D$) | model test | numerical simulation |
|---|---|---|---|---|
| 1 | longitudinal | 0.5 | √ | √ |
| | transverse | | | |
| 2 | longitudinal | 1.0 | √ | √ |
| | transverse | | | |
| 3 | longitudinal | 2.0 | √ | √ |
| | transverse | | | |
| 4 | longitudinal | 3.0 | √ | √ |

### 3.2 Test procedure for model test

The photographs captured during the model test are shown in Fig. 4, and the test procedure can be summarized as the following four steps.

1) Transparent clay was filled into the model test box to a specified depth, and air bubbles were evacuated using a vacuum pump.

2) The entire test device was covered using a black curtain and laser was used to cut a predetermined transverse section. Owing to laser irradiation, the tracer particles resulted in bright spots on the outer wall of the model box.

3) The shield tunneling face was rotated by moving device slowly to move the shield tunneling face back, simulating the instability condition of the shield tunneling face caused by an insufficient support force in actual construction.

4) An industrial camera was used to capture photographs at every half revolution (the shield tunneling face retracted by 0.75 mm, which was 1.5% of the shield diameter) until it rotated ten revolutions.

## 4 Model test results and discussion

### 4.1 Failure mode of different burial depth conditions

#### 4.1.1 Along longitudinal section

Figure 5 shows the failure mode along the longitudinal section of the tunnel under different burial depth conditions. The failure mode under each burial depth condition is the instability region when the shield tunneling face is completely unstable (i.e., when the shield tunneling face displacement reached 12.0% times the tunnel diameter). The displacement of particles in transparent clay was between 0 and 3 mm. The displacement at the blue position was less than 1 mm, and the displacement at the green and red positions was greater than 1 mm in the image. With a limit of 1 mm, the displacement between the blue and green positions changed abruptly, and the macroscopic expression was a line segregating the stability region from the instability region. As shown by the test results in Fig. 5, at $C/D$ = 2.0 and $C/D$ = 3.0, the arching effect occurred in the soil area ranging from 1.5$D$ to 2.0$D$ above the top of the tunnel. This corresponds to approximately 2.0 times the tunnel diameter, based on general experience, indicating that the results of the test based on transparent clay conform to the actual engineering results.

At $C/D$ = 0.5 and $C/D$ = 1.0, the instability region in front of the shield tunneling face developed to the surface, forming a basin-like failure mode. At $C/D$ = 2.0 and $C/D$ =

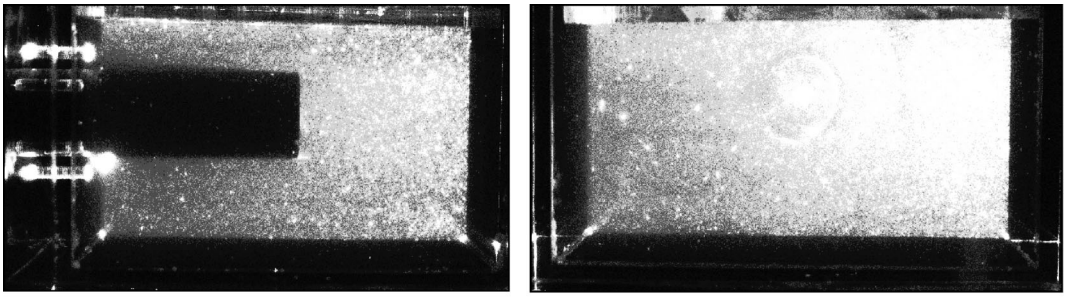

(a) (b)

**Fig. 4** Test photos: (a) along the longitudinal section; (b) along the transverse section.

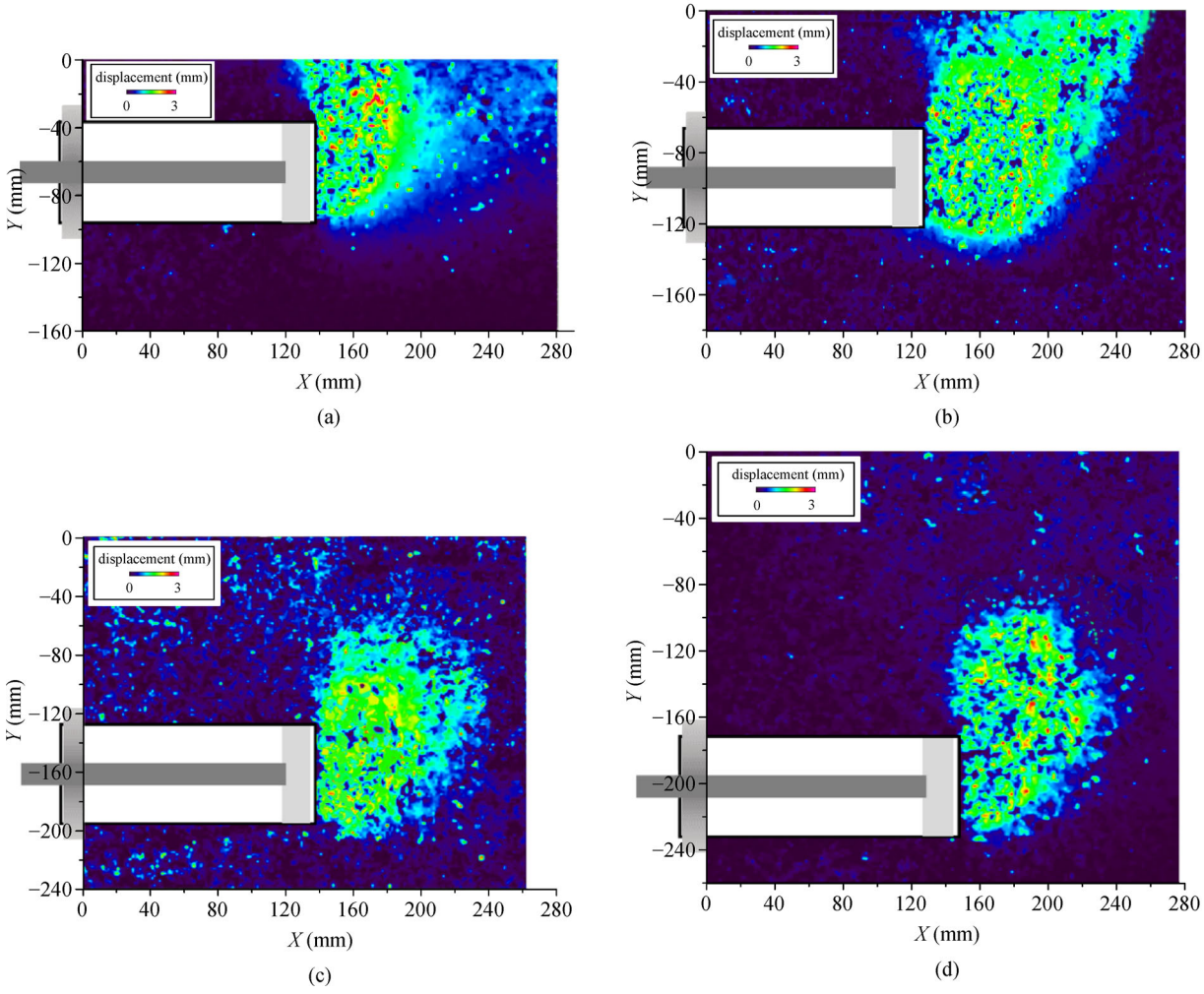


**Fig. 5** Failure mode under different burial depth conditions (longitudinal): (a) $C/D = 0.5$; (b) $C/D = 1.0$; (c) $C/D = 2.0$; (d) $C/D = 3.0$.

3.0, the instability region in front of the shield tunneling face developed to a certain height cutoff, demonstrating the soil arching effect and forming a bulb-like failure mode.

A few scholars [39,48] conducted model tests on sandy soils to investigate the instability of tunnel faces. Figure 6 shows a comparison of these results with those of this study. Some differences were observed between the model tests of clay and sandy soil, manifested as clay developing forward and upward in the influence area as well as the influence area of the sandy soil developing primarily above the tunnel face. The analysis above shows that the results of transparent clay test in this study differ from those of previous transparent sand tests.

#### 4.1.2 Along transverse section

Figure 7 shows the failure mode along the transverse section of the tunnel under different burial depth conditions. At $C/D = 0.5$ and $C/D = 1.0$, the shield tunneling face developed directly along the instability region of the transverse section to the surface, forming a funnel-like failure mode. At $C/D = 2.0$ and $C/D = 3.0$, the instability region developed to a certain height, demonstrating the soil arching effect and forming a local drop-like failure mode. The instability region of the soil arch was in the range $1.5D$–$2.0D$ above the top of the tunnel, consistent with the position where the soil arching effect was observed along the longitudinal section of the tunnel.

As shown in Fig. 8, Mair [49] obtained a funnel-like failure mode of the shield tunneling face instability in clay formations using a centrifugal model test. The studies above show that the change trend of the failure mode along transverse section in this study is consistent with those of previous studies.

### 4.2 Failure mode influence range

#### 4.2.1 Along longitudinal section

Based on the image of the failure mode obtained from the

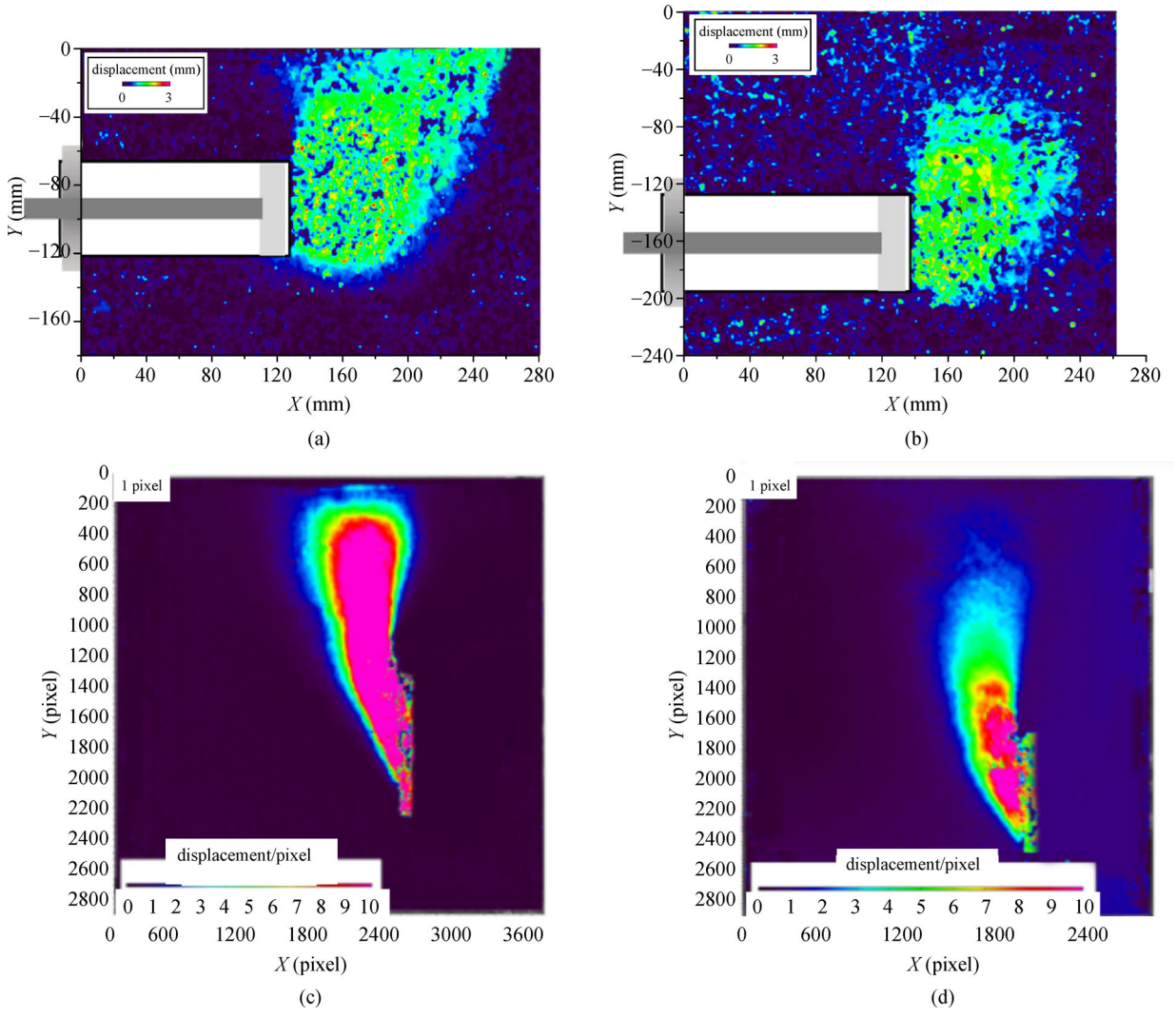


**Fig. 6** Failure mode along the longitudinal section: (a) $C/D = 1.0$; (b) $C/D = 2.0$; (c) $C/D = 1.0$; (d) $C/D = 2.0$ ((c) and (d) are from Ref. [48] with permission).

test, the fracture face is fitted with reference to the logarithmic spiral model [4] used in previous studies. At $C/D$ = 0.5 and $C/D$ = 1.0, the failure mode curve of the shield tunneling face reached the surface directly and can be fitted by an exponential function curve. At $C/D$ = 2.0 and $C/D$ = 3.0, it can be assumed that a soil arch will be formed 0.5$D$ above the tunnel under the failure mode of the shield tunneling face. The failure mode curve can be composed of an exponential function line and a parabola. In Fig. 9, the fitting functions of Figs. 9(a) and 9(b) are $y = a(e^{bx} - 1)$, whereas the fitting functions of Figs. 9(c) and 9(d) are $y = a(e^{bx} - 1)$ and $y = Ax^2 + Bx + 1.5$, respectively. The fitting results were consistent with the test results.

The curve fitting of the failure mode under different burial depths is shown in Table 4, where the relative influence range $\lambda_1$ is the maximum value of the $x$-axis on the fitted curve. The calculation method is shown in Eq. (1), which is derived from the logarithmic spiral. In the equation, when $C/D < 2.0$, $y = 1 + C/D$; when $C/D \geqslant 2.0$, $y = 1.5$.

$$\lambda_1 = \frac{\ln\left(1 + \frac{y}{a}\right)}{b}, \tag{1}$$

where $\lambda_1$ is the relative influence range, $y$ is the $y$-axis value at the surface, and $a$ and $b$ are parameters.

As shown in Table 4, the changes in parameters $a$ and $b$ exhibit a certain regularity. As the burial depth ratio $C/D$ increases, parameter $a$ shows an increasing trend, whereas parameter $b$ shows a decreasing trend. Parameter $A$ has a larger absolute value when $C/D = 3.0$ than when $C/D = 2.0$, indicating that the parabola is more curved. The deeper the tunnel is buried, the more prominent is the soil arch effect.

As the cover depth ratio of $C/D$ increases, the relative influence range $\lambda_1$ increases gradually, but the magnitude

**Table 4** Curve fitting parameter equations and relative influence range (longitudinal)

| cover depth ratio ($C/D$) | parametric equation | parameter | | | | relative influence range $\lambda_1$ |
|---|---|---|---|---|---|---|
| | | $a$ | $b$ | $A$ | $B$ | |
| 0.5 | $y = a(e^{bx} - 1)$ | 0.034 | 2.915 | – | – | 1.307 |
| 1.0 | | 0.086 | 1.950 | – | – | 1.635 |
| 2.0 | $\begin{cases} y = a(e^{bx} - 1), & 0 \leqslant y \leqslant 1.5 \\ y = Ax^2 + Bx + 1.5, & y > 1.5 \end{cases}$ | 0.081 | 1.688 | –0.791 | 1.451 | 1.760 |
| 3.0 | | 0.149 | 1.310 | –1.081 | 1.990 | 1.835 |

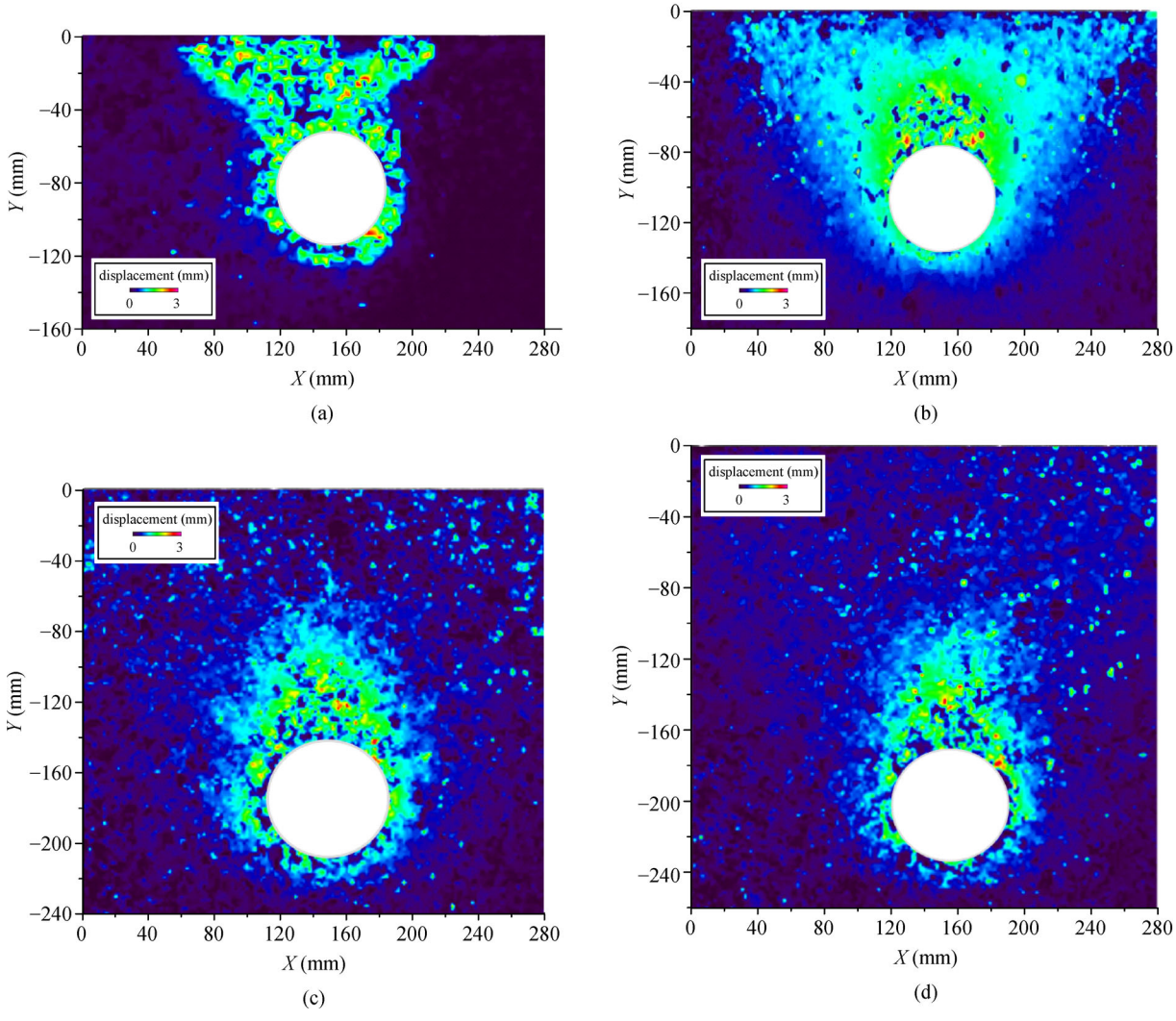


**Fig. 7** Failure mode under different burial depth conditions (transverse): (a) $C/D = 0.5$; (b) $C/D = 1.0$; (c) $C/D = 2.0$; (d) $C/D = 3.0$.

of the increase decreases gradually. Using the burial depth ratio $C/D$ as the $x$-axis and the influence range $\lambda_1$ as the $y$-axis, the curve fitting image is as shown in Fig. 10, and the curve fitting can be obtained using Eq. (2).

$$\lambda_1 = -1.336e^{-1.934(C/D)} + 1.818, \quad (2)$$

where $\lambda_1$ is the relative influence range, and $C/D$ is the burial depth ratio.

As shown in Eq. (2), the relative influence range $\lambda_1$ of the longitudinal section has a limit value of 1.818. This indicates that the instability region caused by the instability of the shield tunneling face in the clay stratum is primarily concentrated in the range of approximately 1.8 times the tunnel diameter in front of the shield tunneling face.

An extreme condition of $C/D = 0$ was assumed, and a slope self-stability analysis was performed to verify the influence range fitting shown in Eq. (2). When the burial

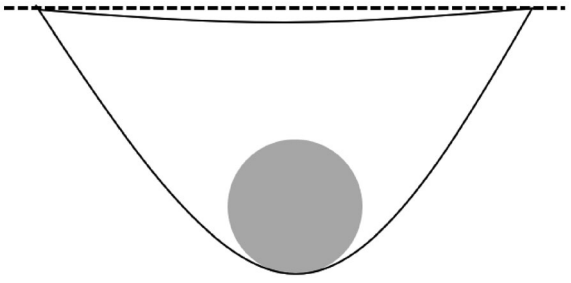

**Fig. 8** Failure mode along transverse section.

depth ratio $C/D$ approached 0, the operating condition transformed into a slope self-stability problem. The relative influence range in front of the shield tunneling face should be $\lambda = m/D = \cot\beta$. The geometric relationship is shown in Fig. 11. According to the stability analysis of a clay slope by Zhang and Liu [51], the stability number method can be used to calculate the self-stabilizing angle $\beta$ of a clay slope. The formula to calculate $N_s$ is shown in Eq. (3).

$$N_s = \frac{c}{\gamma h}, \tag{3}$$

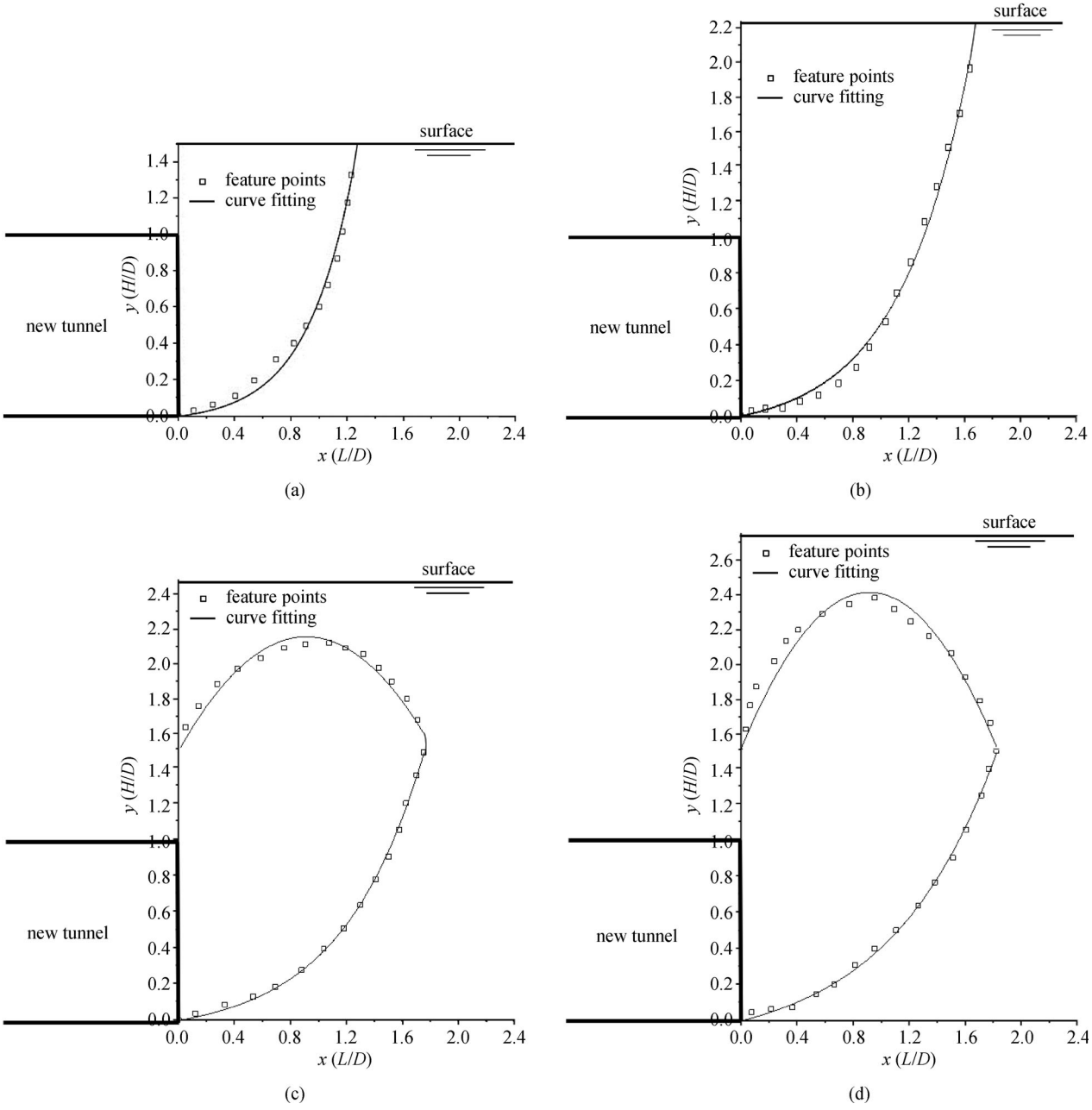


**Fig. 9** Curve fitting of the failure mode (longitudinal): (a) $C/D = 0.5$; (b) $C/D = 1.0$; (c) $C/D = 2.0$; (d) $C/D = 3.0$.

**Table 5** Curve fitting parameter equations and relative influence range (transverse)

| cover depth ratio ($C/D$) | parametric equation | parameter | | | | | relative influence range $\lambda_2$ |
|---|---|---|---|---|---|---|---|
| | | $a$ | $b$ | $A$ | $B$ | $C$ | |
| 0.5 | $y = \pm ax + b$ | 3.195 | –1.311 | – | – | – | 1.760 |
| 1.0 | | 1.445 | –0.409 | – | – | – | 3.334 |
| 2.0 | $\begin{cases} y = \pm A\sqrt{(B-x^2)} + C, & 0 \leqslant y \leqslant 1 \\ y = \pm ax + b, & y > 1 \end{cases}$ | 1.751 | 2 | 1.033 | 0.417 | 0.667 | 1.290 |
| 3.0 | | 2.149 | 2.3 | 1.068 | 0.447 | 0.697 | 1.338 |

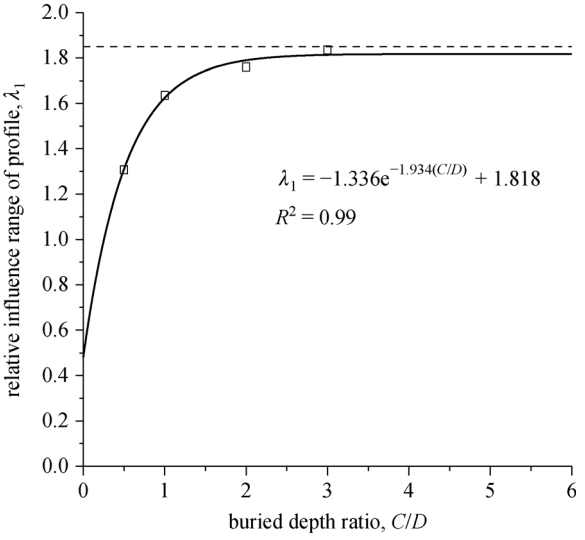


**Fig. 10** Curve fitting of the relationship between $C/D$ and $\lambda_1$.

where $c$ is the soil cohesion, $\gamma$ is the soil bulk density, and $h$ is the slope height.

The accuracy of the formula in the model test was verified through theoretical calculations of engineering projects. The diameter of the tunnel was approximately 6 m. When $h = D = 6$ m, the cohesion of the Tianjin soft clay was $c = 17.6$ kPa, and the bulk density was $\gamma = 17.57$ kN. Hence, $N_s = 0.167$ was obtained. Combined with the internal friction angle $\varphi = 9.3°$, which is approximately 10°, it is shown in Ref. [51] that $\beta = 70°$. When the burial depth ratio $C/D$ approached 0, the relative influence range of the longitudinal section $\lambda_1 = m/D = \cot\beta = 0.364$. Furthermore, substituting $C/D = 0$ into Eq. (2) yielded $\lambda_1 = 0.482$. The $\lambda_1$ values obtained using the two methods were similar, and the difference percentage was 24.48%. Because the stress conditions in the slope stability and shield tunneling face analyses were inconsistent, the calculation results indicated some discrepancies. Comparative analysis studies showed that the fitting of Eq. (2) was reasonable.

### 4.2.2 Along transverse section

The transverse section instability region resembled a funnel or drop. Therefore, a straight line can be used to fit the soil failure mode for $C/D = 0.5$ and $C/D = 1.0$, and an elliptic curve and tangent curve to fit the soil failure mode for $C/D = 2.0$ and $C/D = 3.0$, respectively. The curve fitting is shown in Fig. 12. At $C/D = 2.0$ (Fig. 12 (c)) and $C/D = 3.0$ (Fig. 12 (d)), the soil near the shield tunneling face exhibited a certain soil arching effect. The left and right sides of the image were symmetrically distributed; therefore, the right half was used for analysis. In Fig. 12, the fitting functions of Figs. 12(a) and 12(b) are $y = \pm ax + b$, whereas the fitting functions of Figs. 12(c) and 12(d) are $y = \pm A\sqrt{(B-x^2)} + C$ and $y = \pm ax + b$, respectively. The fitting results were consistent with the test results.

Table 5 shows the curve fittings of the failure modes along the tunnel transverse section under different burial depth conditions. The transverse section relative influence

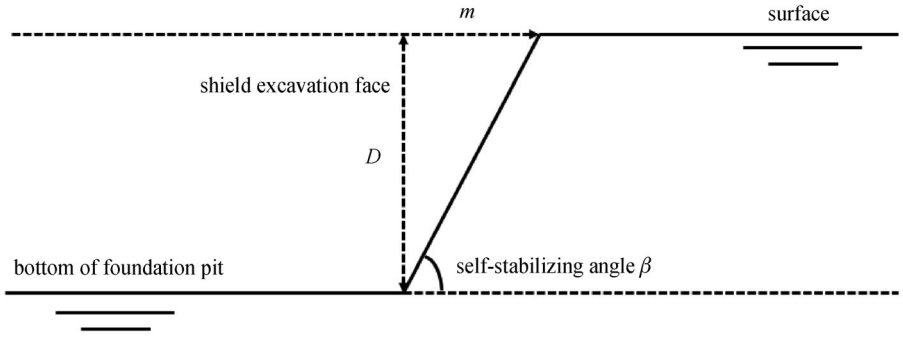


**Fig. 11** Positional relationship between the horizontal distance $m$ and shield diameter $D$.

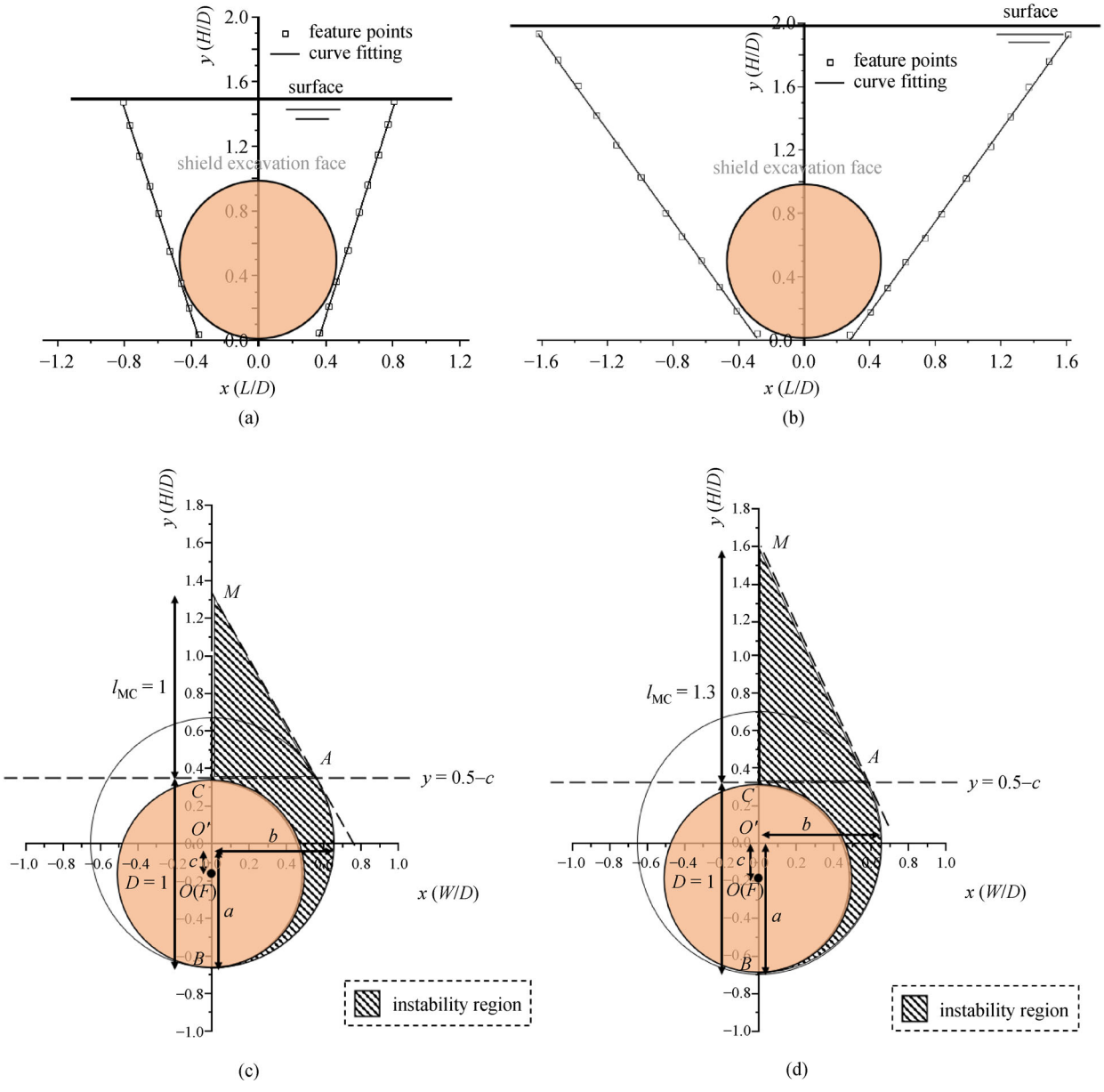


**Fig. 12** Curve fitting of the failure mode (transverse): (a) $C/D = 0.5$; (b) $C/D = 1.0$; (c) $C/D = 2.0$; (d) $C/D = 3.0$.

range $\lambda_2$ is the difference between the maximum and minimum values of the $x$-axis on the fitted curve.

As shown in Table 5, the relative influence range $\lambda_2$ for $C/D = 0.5$ and $C/D = 1.0$ is larger than that for $C/D = 2.0$ and $C/D = 3.0$. This is because at $C/D = 0.5$ and $C/D = 1.0$, a large instability region will develop at the surface. At $C/D = 2.0$ and $C/D = 3.0$, the soil arching effect can occur in the soil, thereby restricting the further development of the instability region.

Comparing the relative influence range along the transverse and longitudinal sections of the tunnel, the relative influence range $\lambda_2$ of the transverse section was larger than $\lambda_1$ at $C/D = 0.5$ and $C/D = 1.0$, and $\lambda_2$ was the same as $\lambda_1$ at $C/D = 2.0$ and $C/D = 3.0$. This is because at $C/D = 0.5$ and $C/D = 1.0$, the influence range of the failure mode in front of the shield tunneling face can develop at the surface. At $C/D = 2.0$ and $C/D = 3.0$, owing to the soil arching effect in the soil, the development of deformation and failure was restricted. The expansion law is the same for the transverse and longitudinal sections.

### 4.3 Support force of shield tunneling face

The support force–displacement relationship curve of the shield tunneling face obtained by monitoring the shield tunneling face support force during the test is shown in Fig. 13(a). The $x$-axis is the relative displacement of the shield tunneling face ($S/D$). The $y$-axis represents the

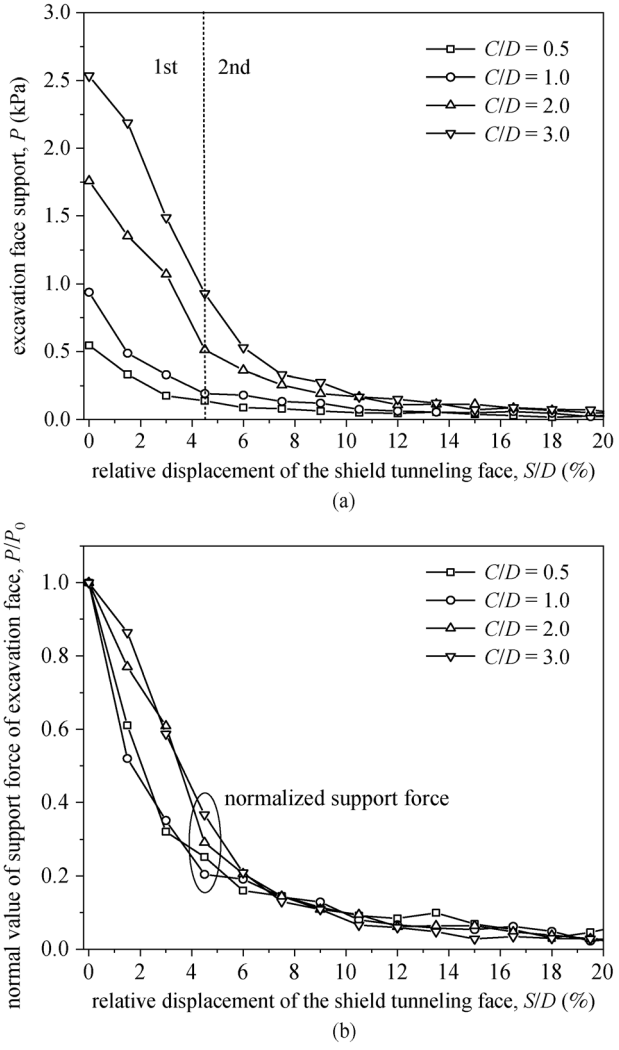


**Fig. 13** Supporting force-displacement relationship of the shield tunneling face: (a) actual value; normalized value.

support force $P$, which can be calculated as follows:

$$P = \frac{4F}{\pi D^2}, \tag{4}$$

where $P$ is the model support force (unit: Pa), $F$ is the sensor reading (unit: N), and $D$ is the model tunnel diameter (unit: m).

Figure 13(a) shows that the support force of the shield tunneling face increases with the burial depth. The formation stress increases with the burial depth; therefore, the support force of the shield tunneling face must be improved accordingly. In addition, with the increase in the displacement of the shield tunneling face, the support force of the shield tunneling face decreased continuously, exhibiting a two-stage feature. In the first stage, the support force decreased rapidly, and the support force decreased slowly in the second stage. The cut-off point for the two stages was approximately 4%. The threshold relative displacement of the shield tunneling face in the clay was approximately 4%.

**Table 6** Particle flow model parameters

| parameter | value |
|---|---|
| normal stiffness $k_n$ (N/m) | 5e7 |
| tangential stiffness $k_s$ (N/m) | 5e7 |
| contact normal stiffness pb_$k_n$ (N/m) | 5e7 |
| contact tangential stiffness pb_$k_s$ (N/m) | 5e7 |
| contact tensile strength pb_ten (Pa) | 3.5e5 |
| contact bonding strength pb_coh (Pa) | 3.5e5 |
| moment transfer coefficient pb_rmul | 0.08 |
| particle friction coefficient fric | 0.05 |
| particle size (m) | 0.002–0.003 |

As shown in Fig. 13(b), to compare the variation law of the support force under the condition of each burial depth, the $y$-axis is represented by $P/P_0$ ($P_0$ is the initial support force). The $P/P_0$ values at each burial depth were similar, showing a two-stage change trend. The support force corresponding to the demarcation point of the two stages is the threshold support force, which is 0.2–0.4 [52]. Hence, the threshold support force in the clay is $0.2P_0$–$0.4P_0$. In addition, the threshold support force differs slightly at different depths, and the threshold support force tends to increase linearly with the burial depth. The deeper the burial depth, the greater is the formation pressure, and hence the greater is the support force required to maintain the stability of the shield tunneling face.

## 5 Numerical simulation

### 5.1 Parameter calibration

Conventionally, the stability of a shield tunneling face can be analyzed using the FEM and DEM. The FEM offers many advantages, and numerous significant research results regarding shield stability have been obtained using this method [53–55]. Owing to the discrete characteristics of soft clay particles in actual engineering, the DEM was used in this study to analyze the spatial movement law of the surrounding soil during active failure. Using the trial-and-error method in PFC$^{3D}$ software, the mesoscopic parameters such as the particle contact stiffness, friction coefficient, and bond strength were continuously adjusted until the selected parameters can simulate a stress-strain curve that is consistent with that of transparent clay.

Figure 14(a) shows the sample generated during the parameter calibration. It measured 39.1 mm in diameter and 80 mm in height, consistent with the size of the transparent clay sample used in the laboratory triaxial test. A comparison between the stress-strain curves obtained from PFC$^{3D}$ and the triaxial tests is shown in Fig. 14(b).

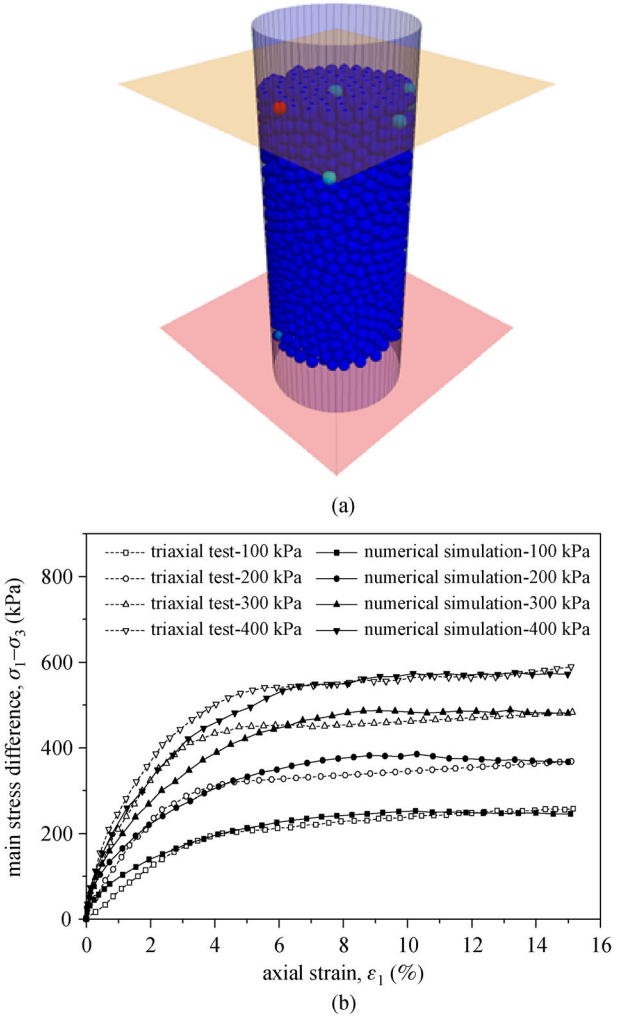


**Fig. 14** Parameter calibration: (a) triaxial sample from particle flow; (b) stress-strain curves between the numerical simulation and triaxial test.

The specific parameters of the PFC$^{3D}$ numerical model are listed in Table 6. The numerically simulated curve is consistent with the results of the triaxial test. Therefore, the parameters in Table 6 can be used to establish a numerical model for the failure mode of the shield tunneling face.

## 5.2 Established model

The initial model was generated using the radius expansion method. After applying gravity acceleration, an automatic balance calculation was performed. The termination condition is that the overall average change ratio ("Aratio" in the software) of the model is less than 1e–5. The condition of the model after the initial *in situ* stress balance is shown in Fig. 15(a). The different colors of the particles correspond to the different radii. As shown, particles with different particle sizes mixed uniformly, reflecting a better grading effect. The analysis of numerical simulation results in the following are based on Fig. 15(a). Tunnel excavation was simulated by deleting the particles inside the tunnel. The lining was simulated by a cylindrical wall, and the grouting layer was simulated using the parameters of the strengthened soil, i.e., the increased strength and stiffness of the soil in the grouting layer. Furthermore, a circular wall was added at the location of the shield tunneling face, the diameter of which was the same as the tunnel diameter, to simulate the support of the shield tunneling face. The development process of failure was simulated by slowly retreating the wall (0.00075 m/time step) at the shield tunneling face. The contact force on the wall at the shield tunneling face served as the support force during the shield instability and was monitored. The simulation instability process caused by the retreating shield tunneling face is shown in Fig. 15(b).

## 5.3 Results and discussion

### 5.3.1 Comparison of failure modes between numerical simulation and model test

The failure modes of the shield tunneling face at $C/D = 0.5$ are shown in Fig. 16. PFC$^{3D}$ can simulate large deformations and large displacements accurately. When the shield tunneling faced backward, the soil entered the tunnel; this phenomenon can be observed from the longitudinal section view. In the model test, the tunnel irradiated by the laser was opaque. Although the soil particles had entered the tunnel, the inside of the tunnel was not visible from the longitudinal section. The failure modes of the numerical simulation were consistent with those of the model test, and they were all integrated failure modes that extended to the surface. The longitudinal influence range of the numerical simulation was approximately 1.5$D$, which was similar to that of the model test (1.307$D$). Therefore, it can be concluded that the selection of soil parameters in the numerical calculation model was reasonable.

### 5.3.2 Failure mode of different burial depth conditions

Figure 17 shows the failure mode along the longitudinal section of the tunnel under different burial depth conditions. At $C/D = 0.5$ and $C/D = 1.0$, the instability range reached the surface directly, forming an overall basin-like failure mode. At $C/D = 2.0$, the instability range could not be extended to the surface, and a bulb-like soil arch with a range of 1 to 2$D$ formed near the shield tunneling face. The numerical simulation test results were consistent with the previous model test results.

### 5.3.3 Surface settlement

Figure 18 shows the normalized surface settlement curves along the transverse section under different burial depth

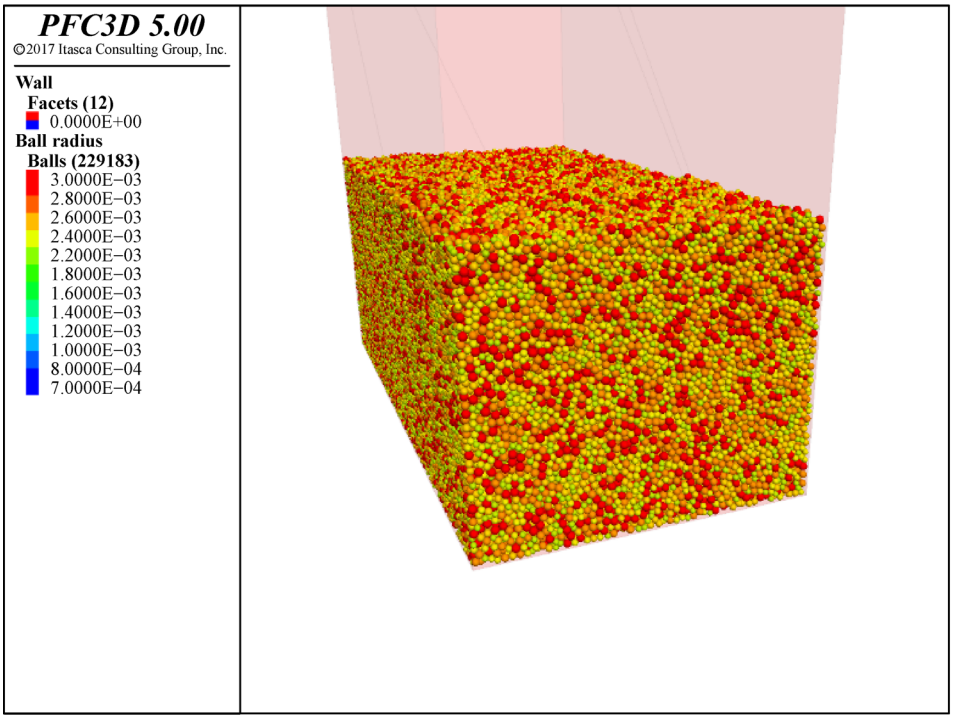


(a)

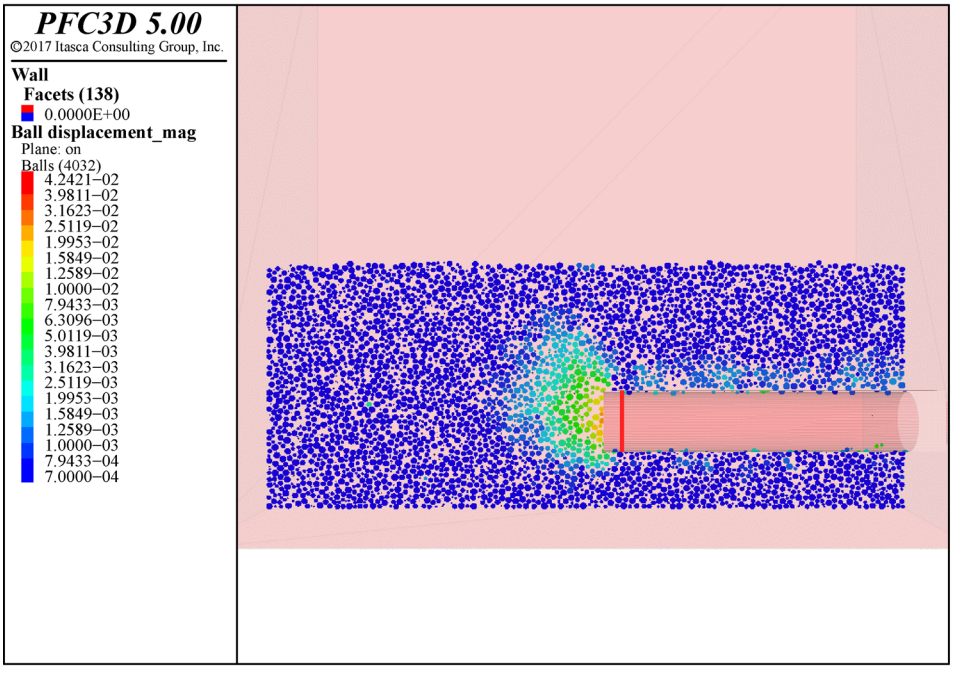


(b)

**Fig. 15** Numerical simulation model: (a) numerical model after *in-situ* stress balance; (b) simulation instability process of the shield tunneling face.

conditions. The surface settlement of the three curves increased gradually from both sides to the middle of the tunnel. At $C/D = 2.0$ and $C/D = 1.0$, the surface settlement decreased by 36.24% and 58.23%, respectively, compared with that at $C/D = 3.0$. The results show that with increasing tunnel depth, the surface settlement reduced significantly. This is because as the burial depth increased, the overburden layer demonstrated an enhanced buffering capacity for soil deformation.

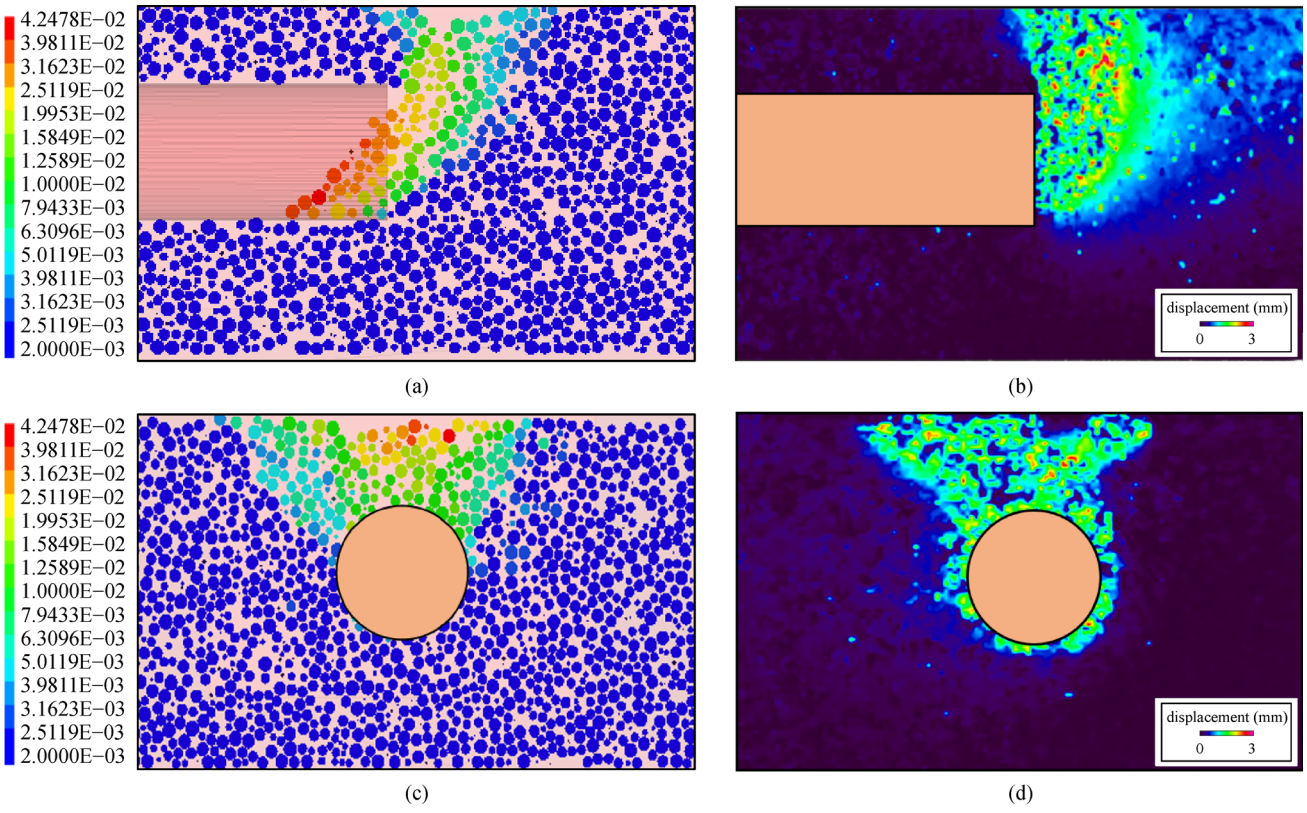


**Fig. 16** Comparison of failure modes: (a) numerical simulation along the longitudinal section; (b) model test along the longitudinal section; (c) numerical simulation along the transverse section; (d) model test along the transverse section.

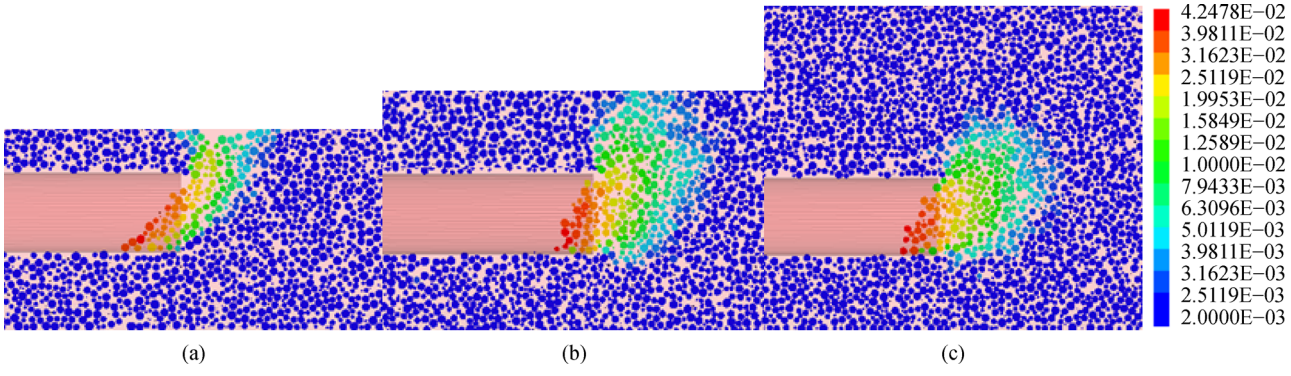


**Fig. 17** Failure mode under different burial depth conditions (longitudinal): (a) $C/D = 0.5$; (b) $C/D = 1.0$; (c) $C/D = 2.0$.

5.3.4 Comparison between numerical simulation and Peck formula

Based on the statistical results of a large amount of measured data, Peck [56] hypothesized that surface settlement was caused by soil loss. Under the assumption that the soil is undrained and the volume of the settlement tank is equal to the volume of the soil loss, the ground settlement tank distribution is similar to a normal distribution. The formulas to estimate the transverse section ground subsidence are shown in Eqs. (5) and (6).

$$s(x) = s_{\max}\exp[-x^2/(2i^2)], \tag{5}$$

$$s_{\max} = \frac{V_{\text{loss}}}{i\sqrt{2\pi}} = \frac{\pi D^2 \eta}{i\sqrt{2\pi}}, \tag{6}$$

where $x$ is the horizontal distance from the transverse section of the tunnel, $s(x)$ is the ground settlement at position $x$, $s_{\max}$ is the maximum surface settlement above the tunnel axis, $V_{\text{loss}}$ is the soil loss per unit length, $\eta$ is the soil loss rate, $D$ is the outer radius of the tunnel, and $i$ is the width coefficient of the ground subsidence tank.

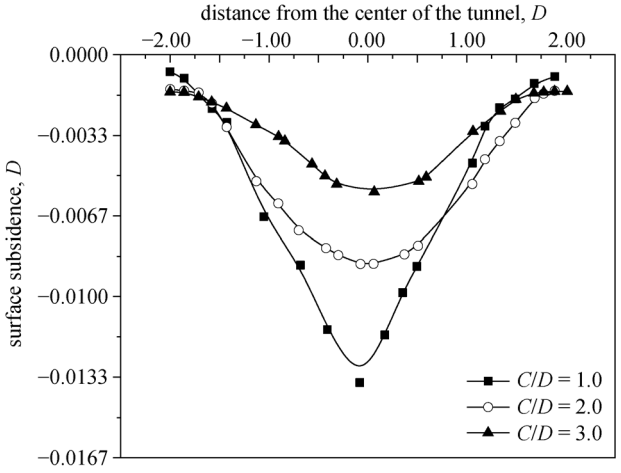


**Fig. 18** Normalized surface settlement curves.

According to Knothe [57], the parameter $i$ depends on the strength of the stratum close to the surface, as well as the tunnel depth and radius. The formula to calculate $i$ is shown in Eq. (7).

$$i = \frac{h}{\sqrt{2\pi}\tan\left(45° - \frac{\varphi}{2}\right)}, \tag{7}$$

where $h$ is the depth from the surface to the center of the tunnel, and $\varphi$ is the angle of internal friction.

Previous studies have suggested the typical expected soil loss $\eta$ during shield tunneling of approximately 2.25% [58,59]. Hence, the soil loss $\eta$ was set to 2.25% in this study. According to the relevant parameters of transparent soil shown in Table 2 and the diameter and burial depth of the shield tunnel in the model test, the settlement curves under different tunnel burial depth conditions can be calculated, as shown in Fig. 19. In addition, many methods can be used to calculate $i$, of which the typical method is to use. In this study, $k$ was set as 0.5 in the formula (based on the characteristics of Tianjin clay). The calculation results were compared with other results, as shown in Fig. 19.

$$i = kh, \tag{8}$$

where $k$ is an empirical constant of proportionality ranging between 0.4 and 0.7 for cohesive soils [58].

Based on a comparative analysis of Fig. 19, the result calculated using Eq. (7) differed slightly from that simulated for $C/D$ = 1.0, whereas the result calculated using Eq. (8) differed slightly from that simulated for $C/D$ = 3.0. In other conditions, the results of the numerical simulation were consistent with those calculated using the Peck formula. In general, with increasing burial depth, the surface settlement value decreased continuously. These curves exhibited a normal distribution and were similar to the numerical simulation results.

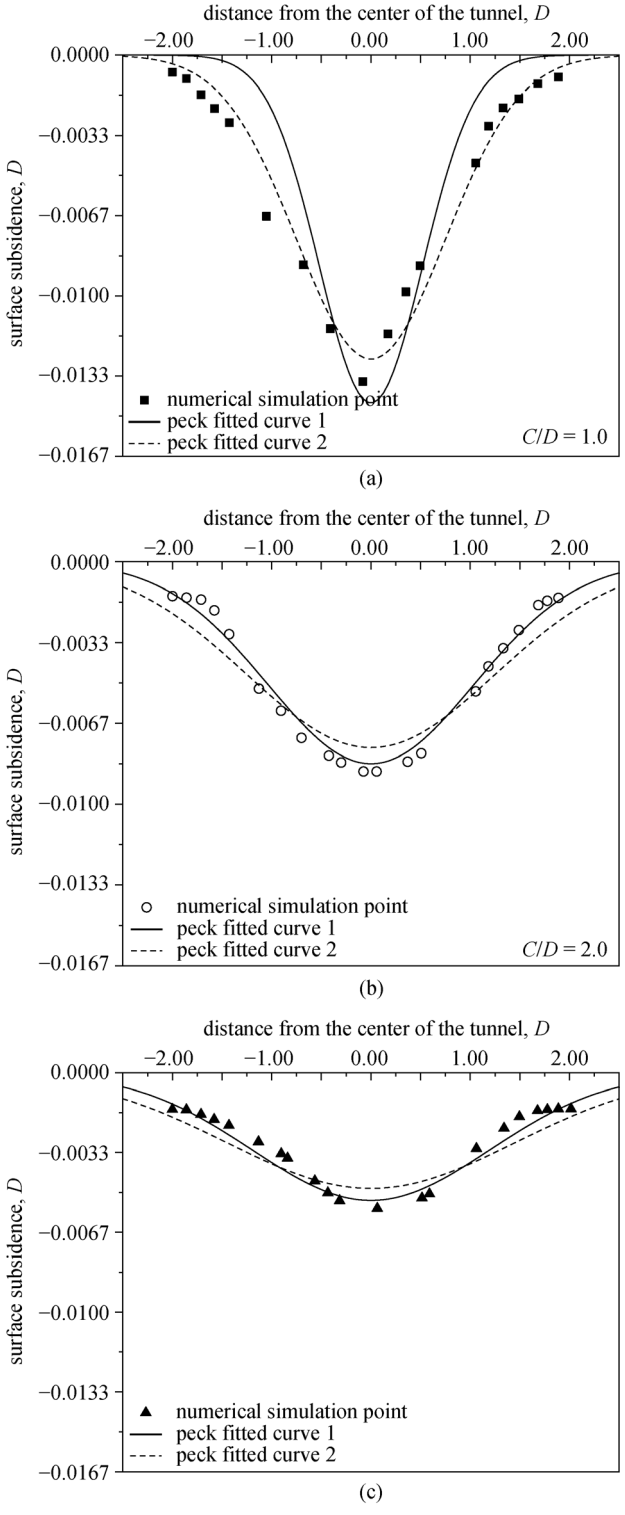


**Fig. 19** Comparison of the numerical simulation and peck curve on the transverse section: (a) $C/D$ = 1.0; (b) $C/D$ = 2.0; (c) $C/D$ = 3.0.

## 6 Conclusions

Herein, an experimental model system was proposed for

analyzing the stability of a shield tunneling face using a type of transparent clay reflecting the engineering characteristics of Tianjin soft clay. The system was used to investigate the stability of the shield tunneling face to solve the "black box" problem and directly observe the internal displacement of the soil under active failure. In addition, an accurate function was performed to express the active failure mode of the shield tunneling face, and the relative influence range was deduced.

Considering the particle migration law, a DEM software, namely, PFC$^{3D}$, was employed to further analyze the active failure mode of the shield tunneling face and surface settlement under different burial depth conditions. Compared with the model test, the PFC$^{3D}$ simulated the movement of soil particles in the inner tunnel when active failure occurred.

**Acknowledgements** The study described herein was financially supported by the National Key Research and Development Program of China (No. 2017YFC0805402) and the Open Project of the State Key Laboratory of Disaster Reduction in Civil Engineering (No. SLDRCE17-01). All support received is appreciated.

## References

1. Horn N. Horizontal earth pressure on the vertical surfaces of the tunnel tubes. In: Proceedings of the National Conference of the Hungarian Civil Engineering Industry. Budapest, Hungary, 1961 (in German)
2. Murayama S, Endo M, Hashiba T, Yamamoto K, Sasaki H. Geotechnical aspects for the excavating performance of the shield machines. In: The 21st Annual Lecture in Meeting of Japan Society of Civil Engineers. Tokyo, Japan, 1966
3. Jancsecz S, Steiner W. Face Support for a Large Mix-Shield in Heterogeneous Ground Conditions. Tunnelling'94. Boston, MA: Springer, 1994, 531–550
4. Belter B, Heiermann W, Katzenbach R, Maidl B, Quick H, Wittke W. New concepts for realization of infrastructural projects. Bauingenieur, 1999, 74(1): 1–7 (in German)
5. Wei G, He F. Calculation of minimal support pressure acting on shield face during pipe jacking in sandy soil. Chinese Journal of Underground Space and Engineering, 2007, 3(5): 903–908 (in Chinese)
6. Hu W T, Lü X L, Huang M S. Three-dimensional limit equilibrium solution of the support pressure on the shield tunnel face. Chinese Journal of Underground Space and Engineering, 2011, 7(5): 853–856 (in Chinese)
7. Broms B B, Bennermark H. Stability of clay at vertical openings. Journal of the Soil Mechanics and Foundations Division, ASCE, 1967, 96(1): 71–94.
8. Davis E H, Gunn M J, Mair R J, Seneviratine H N. The stability of shallow tunnels and underground openings in cohesive material. Geotechnique, 1980, 30(4): 397–416
9. Leca E, Dormieux L. Upper and lower bound solutions for the face stability of shallow circular tunnels in frictional material. Geotechnique, 1990, 40(4): 581–606
10. Lü X L, Wang H R, Huang M S. Limit theoretical study on face stability of shield tunnels. Chinese Journal of Geotechnical Engineering, 2011, 33(1): 57–62 (in Chinese)
11. Kirsch A. Experimental investigation of the face stability of shallow tunnels in sand. Acta Geotechnica, 2010, 5(1): 43–62
12. Chen R P, Li J, Chen Y M, Kong L G. Large-scale tests on face stability of shield tunnelling in dry cohesionless soil. Chinese Journal of Geotechnical Engineering, 2011, 33(1): 117–122 (in Chinese)
13. Vlachopoulos N, Vazaios I, Madjdabadi B M. Investigation into the influence of excavation of twin-bored tunnels within weak rock masses adjacent to slopes. Canadian Geotechnical Journal, 2018, 55(11): 1533–1551
14. Lu X L, Zhou Y C, Li F D. Centrifuge model test and numerical simulation of stability of excavation face of shield tunnel in silty sand. Rock and Soil Mechanics, 2016, 37(11): 3324–3328 (in Chinese)
15. di Prisco C, Flessati L, Frigerio G, Castellanza R, Caruso M, Galli A, Lunardi P. Experimental investigation of the time-dependent response of unreinforced and reinforced tunnel faces in cohesive soils. Acta Geotechnica, 2018, 13(3): 651–670
16. Zhou S W, Zhuang X Y, Zhu H H, Rabczuk T. Phase field modelling of crack propagation, branching and coalescence in rocks. Theoretical and Applied Fracture Mechanics, 2018, 96: 174–192
17. Zhou S W, Zhuang X Y, Rabczuk T. Phase field modeling of brittle compressive-shear fractures in rock-like materials: A new driving force and a hybrid formulation. Computer Methods in Applied Mechanics and Engineering, 2019, 355: 729–752
18. Zhuang X Y, Zhou S W, Sheng M, Li G S. On the hydraulic fracturing in naturally-layered porous media using the phase field method. Engineering Geology, 2020, 266: 105306
19. Manouchehrian A, Marji M F, Mohebbi M. Comparison of indirect boundary element and finite element methods. Frontiers of Structural and Civil Engineering, 2012, 6(4): 385–392
20. Li Z L, Soga K, Wright P. Three-dimensional finite element analysis of the behaviour of cross passage between cast-iron tunnels. Canadian Geotechnical Journal, 2016, 53(6): 930–945
21. Chen R P, Zhang P, Wu H N, Wang Z T, Zhong Z Q. Prediction of shield tunneling-induced ground settlement using machine learning techniques. Frontiers of Structural and Civil Engineering, 2019, 13(6): 1363–1378
22. Liu C, Pan L F, Wang F, Zhang Z X, Cui J, Liu H, Duan Z, Ji X Y. Three-dimensional discrete element analysis on tunnel face instability in cobbles using ellipsoidal particles. Materials (Basel), 2019, 12(20): 3347
23. Vazaios I, Vlachopoulos N, Diederichs M S. Mechanical analysis and interpretation of excavation damage zone formation around deep tunnels within massive rock masses using hybrid finite-discrete element approach: Case of Atomic Energy of Canada Limited (AECL) Underground Research Laboratory (URL) test tunnel. Canadian Geotechnical Journal, 2019, 56(1): 35–59
24. Zhang Y M, Zhuang X Y, Lackner R. Stability analysis of shotcrete

supported crown of NATM tunnels with discontinuity layout optimization. International Journal for Numerical and Analytical Methods in Geomechanics, 2018, 42(11): 1199–1216
25. Sun Z Z, Zhang Y M, Yuan Y, Mang H A. Stability analysis of a fire-loaded shallow tunnel by means of a thermo-hydro-chemo-mechanical model and discontinuity layout optimization. International Journal for Numerical and Analytical Methods in Geomechanics, 2019, 43(16): 2551–2564
26. Yan X, Sun Z Z, Li S C, Liu R T, Zhang Q S, Zhang Y M. Quantitatively assessing the pre-grouting effect on the stability of tunnels excavated in fault zones with discontinuity layout optimization: A case study. Frontiers of Structural and Civil Engineering, 2019, 13(6): 1393–1404
27. Rabczuk T, Belytschko T. Cracking particles: A simplified meshfree method for arbitrary evolving cracks. International Journal for Numerical Methods in Engineering, 2004, 61(13): 2316–2343
28. Rabczuk T, Zi G, Bordas S, Nguyen-Xuan H. A simple and robust three-dimensional cracking-particle method without enrichment. Computer Methods in Applied Mechanics and Engineering, 2010, 199(37–40): 2437–2455
29. Mannheimer R J, Oswald C J. Development of transparent porous-media with permeabilities and porosities comparable to soils, aquifers, and petroleum reservoirs. Ground Water, 1993, 31(5): 781–788
30. Ahmed M, Iskander M. Transparent soil model tests and FE analyses on tunneling induced ground settlement. In: Geo-Frontiers 2011: Advances in Geotechnical Engineering. Virginia: ASCE, 2011, 3381–3390
31. Gong Q M, Zhou J H, Zhou S H, Ji C. Strength property and feasibility test of transparent soil to model clayey soil. Journal of Tongji University (Natural Science), 2016, 44(6): 853–860
32. Kong G Q, Li H, Yang Q, Meng Y D, Xu X L. Cyclic undrained behavior and liquefaction resistance of transparent sand manufactured by fused quartz. Soil Dynamics and Earthquake Engineering, 2018, 108: 13–17
33. De Guzman E M B, Alfaro M C. Laboratory-scale model studies on corduroy-reinforced road embankments on peat foundations using transparent soil. Transportation Geotechnics, 2018, 16: 1–10
34. Kong G Q, Li H, Yang G, Cao Z H. Investigation on shear modulus and damping ratio of transparent soils with different pore fluids. Granular Matter, 2018, 20(1): 8
35. Wang J X, Liu X T, Liu S L, Zhu Y F, Pan W Q, Zhou J. Physical model test of transparent soil on coupling effect of cut-off wall and pumping wells during foundation pit dewatering. Acta Geotechnica, 2019, 14(1): 141–162
36. Iskander M, Liu J Y. Spatial deformation measurement using transparent soil. Geotechnical Testing Journal, 2010, 33(4): 314–321
37. Chen J F, Guo X P, Xue J F, Guo P H. Load behaviour of model strip footings on reinforced transparent soils. Geosynthetics International, 2019, 26(3): 251–260
38. Sun J Z, Liu J Y. Visualization of tunnelling-induced ground movement in transparent sand. Tunnelling and Underground Space Technology, 2014, 40: 236–240
39. Lü X L, Zhou Y C, Huang M S, Zeng S. Experimental study of the face stability of shield tunnel in sands under seepage condition. Tunnelling and Underground Space Technology, 2018, 74: 195–205
40. Xiang Y Z, Liu H L, Zhang W G, Chu J, Zhou D, Xiao Y. Application of transparent soil model test and DEM simulation in study of tunnel failure mechanism. Tunnelling and Underground Space Technology, 2018, 74: 178–184
41. Gong Q M, Zhao Y, Zhou J H, Zhou S H. Uplift resistance and progressive failure mechanisms of metro shield tunnel in soft clay. Tunnelling and Underground Space Technology, 2018, 82: 222–234
42. Yuan B X, Sun M, Wang Y X, Zhai L H, Luo Q Z, Zhang X Q. Full 3D displacement measuring system for 3D displacement field of soil around a laterally loaded pile in transparent soil. International Journal of Geomechanics, 2019, 19(5): 04019028
43. Lei H Y, Liu Y N, Zhai S B, Tu C K, Liu M. Visibility and mechanical properties of transparent clay. Chinese Journal of Geotechnical Engineering, 2019, 41(S2): 53–56 (in Chinese)
44. Zhang Y P, Li L, Wang S Z. Experimental study on pore fluid for forming transparent soil. Journal of Zhejiang University (Engineering Science), 2014, 48(10): 1828–1834 (in Chinese)
45. Lei H Y, Ren Q, Lu H B, Li B. Research on consolidation property of double layer soft clay foundation under different relative thickness conditions. Chinese Journal of Underground Space and Engineering, 2018, 14(3): 705–711 (in Chinese)
46. Hong Z S, Onitsuka K. A method of correcting yield stress and compression index of Ariake clays for sample disturbance. Soils and foundations, 1998, 38(2): 211–222
47. Hong Z S, Liu S Y, Yu X J. On destructuration of structured soils. Rock and Soil Mechanics, 2004, 25(5): 684–687 (in Chinese)
48. Sun X H, Miao L C, Lin H S. Arching effect of soil ahead of working face in shield tunnel in sand with various depths. Rock and Soil Mechanics, 2017, 38(10): 2980–2988 (in Chinese)
49. Mair R J. Centrifugal Modelling of Tunnel Construction in Soft Clay. Cambridge: Cambridge University, 1978
50. Franza A, Marshall A M, Zhou B, Shirlaw N, Boone S. Greenfield tunnelling in sands: The effects of soil density and relative depth. Geotechnique, 2018, 69(4): 297–307
51. Zhang K G, Liu S Y. Soil Mechanics. Beijing: China Architecture & Building Press, 2010 (in Chinese)
52. Ahmed M, Iskander M. Evaluation of tunnel face stability by transparent soil models. Tunnelling and Underground Space Technology, 2012, 27(1): 101–110
53. Zhou S W, Rabczuk T, Zhuang X Y. Phase field modeling of quasi-static and dynamic crack propagation: COMSOL implementation and case studies. Advances in Engineering Software, 2018, 122: 31–49
54. Zhou S W, Zhuang X Y, Rabczuk T. A phase-field modeling approach of fracture propagation in poroelastic media. Engineering Geology, 2018, 240: 189–203
55. Zhou S W, Zhuang X Y, Rabczuk T. Phase-field modeling of fluid-driven dynamic cracking in porous media. Computer Methods in Applied Mechanics and Engineering, 2019, 350: 169–198
56. Peck R B. Deep excavations and tunneling in soft ground. In: Proceedings of the 7th International Conference on Soil Mechanics and Foundation Engineering. Mexico, 1969: 225–290

57. Knothe S. Observations of surface movements under influence of mining and their theoretical interpretation. In: Proceedings of the European congress on ground movement. Leeds: University of Leeds, 1957, 210–218
58. Mair R J, Taylor R N. Theme lecture: Bored tunnelling in the urban environment. In: Proceedings of the Fourteenth International Conference on Soil Mechanics and Foundation Engineering. balkema, Hamburg, 1997, 2353–2385
59. Hung C J, Monsees J, Munfah N, Wisniewski J. Technical Manual for Design and Construction of Road Tunnels. Report to US Department of Transportation prepared by Parsons Brinckerhoff, Inc. FHWA-NHI-09–010. 2009